Journal of Power Sources 201 (2012) 112–120

Contents lists available at SciVerse ScienceDirect

Journal of Power Sources

journal homepage: www.elsevier.com/locate/jpowsour

# Combined Cr and S poisoning in solid oxide fuel cell cathodes

J. Andreas Schuler[a,b,*], Harumi Yokokawa[c], Caroline F. Calderone[b], Quentin Jeangros[b], Zacharie Wuillemin[a], Aïcha Hessler-Wyser[b], Jan Van herle[a]

[a] Laboratoire d'Energétique Industrielle (LENI), Ecole Polytechnique Fédérale de Lausanne (EPFL), CH-1015 Lausanne, Switzerland
[b] Centre Interdisciplinaire de Microscopie Electronique (CIME), Ecole Polytechnique Fédérale de Lausanne (EPFL), CH-1015 Lausanne, Switzerland
[c] National Institute of Advanced Industrial Science and Technology (AIST), 305-8565 Ibaraki, Japan

ARTICLE INFO

*Article history:*
Received 17 August 2011
Received in revised form 27 October 2011
Accepted 31 October 2011
Available online 9 November 2011

*Keywords:*
Solid oxide fuel cell
Cathode
Degradation
Chromium
Sulfur
Cr-poisoning

ABSTRACT

This work aims to compare the effect of combined chromium and sulfur contaminating conditions to the Cr contamination alone on the Cr poisoning mechanisms in $(La,Sr)MnO_3$-$(Zr,Y)O_2$ solid oxide fuel cell (SOFC) cathodes. Whereas $Cr_2O_3$ and $(Cr,Mn)_3O_4$ are found at active triple phase boundaries under the Cr-poisoning condition, the formation of $SrCrO_4$ is promoted under combined Cr and S contaminating conditions, where Cr accumulations act as getters incorporating sulfur, to form $Sr(Cr,S)O_4$ compounds. The identification of this phase is validated on the synthesized and simulated species by scanning/transmission electron microscopy (SEM/TEM) techniques; its possible formation is predicted by thermodynamic analysis of the stability of perovskite compounds in the presence of combined Cr and S polluting conditions. In contrast, sulfur alone is not found to poison active sites in these composite cathodes. These findings suggest that the Cr poisoning degradation mechanism is altered when $(La,Sr)MnO_3$ is exposed to Cr vapors in the presence of sulfur contamination; the access to electrochemical active sites may be hindered by the formation of $Sr(Cr,S)O_4$ in a similar manner to a Cr-getter effect in $(La,Sr)(Co,Fe)O_3$ cathodes.



## 1. Introduction

Since the early seventies, Sr-doped perovskites have been suggested as substitutes to noble metals as lower cost electrode materials for fuel cells [1] and for the catalytic treatment of exhaust gas [2]. However, perovskites suffer from limitations in their applicability in some industrial processes, in particular from their susceptibility to poisoning by sulfur dioxide [3]. Originally proposed as potential automotive catalysts, the early perovskite compositions, mostly manganites and cobaltites, have failed to become practical because of their low resistance to sulfur, i.e. low temperature stable sulfate formation occurs [4,5].

In the field of solid oxide fuel cells (SOFCs), where sulfur in the fuel is a known issue [6], less attention was brought so far to sulfur on the cathode side, as only a trace of $SO_2$, in the ppb range, is found in environmental air [7]. Recently, Yamaji et al. as well as Liu et al. showed high tolerance of $(La,Sr)MnO_3$-based cathodes (LSM) towards deliberate S contamination [8–10], suggesting that S-poisoning is not a barrier in optimized manganite compositions [5]. In contrast to LSM cathodes, sulfur contamination significantly affects the cathode performance of $(La,Sr)(Co,Fe)O_3$ (LSCF) or related active cathodes [8–10]. In this sense, the chemical stability of the cathode is directly related to the degradation in the presence of sulfur.

A contrasting situation is found in the so-called Cr-poisoning phenomenon, i.e. cathode degradation is caused by its accumulation of Cr vapor species generated by Cr-containing cell-proximal stack compounds. LSM, which is the most stable composition among the perovskite cathodes, undergoes the most severe Cr poisoning degradation as Cr vapors are preferentially deposited on electrochemical active sites. Contrariwise, in LSCF cathodes, where the major effect is recognized as $SrCrO_4$ formation near the cathode surface and remote from the active sites, Cr-poisoning is less severe [11].

The investigation of differences between these two contaminations Cr and S and plausible combined effects is therefore of interest. Nevertheless, testing of cathode poisoning by sulfur remains scarce, especially in the stack configuration, where S contamination arises in combination with other pollutant species. This study addresses this specific point, by prospecting the effect of combined Cr and S poisoning in SOFC cathodes. It was based on the observation of having identified Sr/Cr/S-oxides in stack post-test samples, reported earlier [12–14].

In these previous studies, $Cr_2O_3/MnCr_2O_4$ phases in the $LSM/(Y,Zr)O_2$ composite cathode as well as $SrCrO_4$ and $SrSO_4$ phases in the $(La,Sr)(Co)O_3$ (LSC) current collection layer (CCL) were

* Corresponding author at: Laboratoire d'Energétique Industrielle (LENI), Ecole Polytechnique Fédérale de Lausanne (EPFL), CH-1015 Lausanne, Switzerland. Tel.: +41 021 693 4827; fax: +41 021 693 3502.
*E-mail address:* andreas.schuler@epfl.ch (J.A. Schuler).

0378-7753/$ – see front matter © 2011 Elsevier B.V. All rights reserved.
doi:10.1016/j.jpowsour.2011.10.123

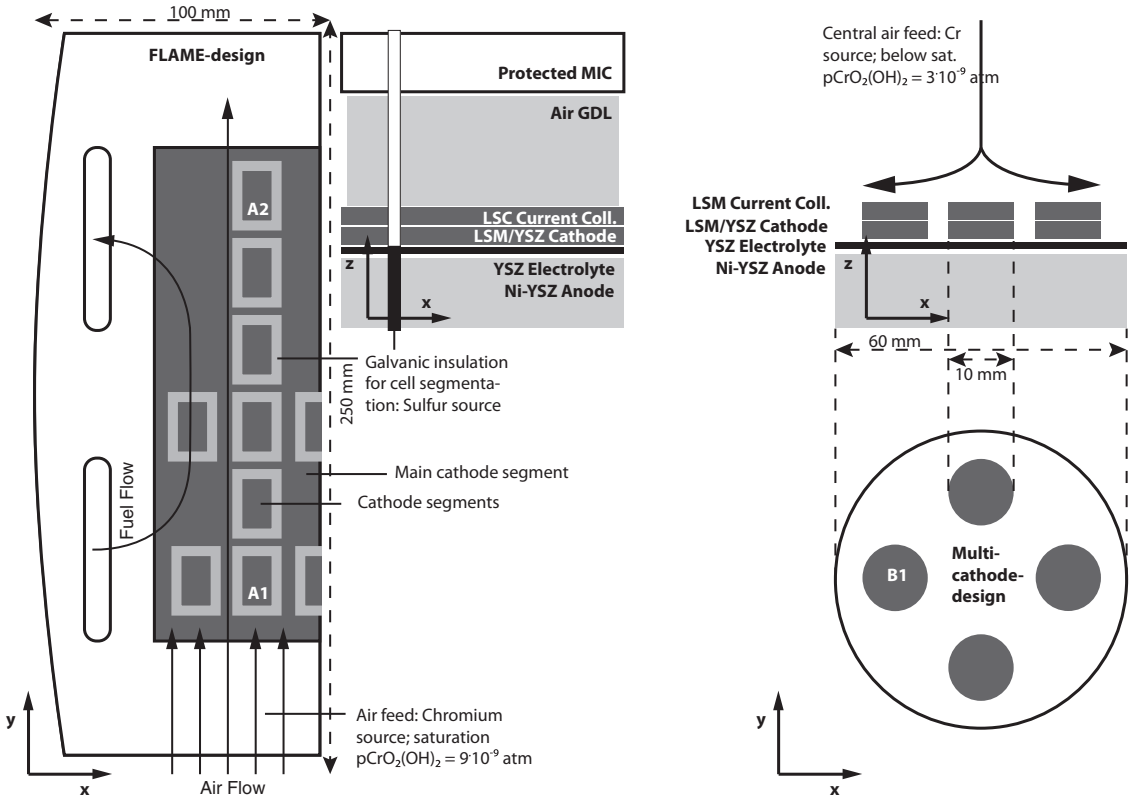


**Fig. 1.** Schematic description of Cr contaminating conditions, in combination with S for type A cell (segmented 1-cell stack; left) or for Cr alone for type B cell (multicathode button cell; right), respectively. The S-containing insulating paste for segmentation of type A cell generated increasing S concentrations along the airflow in the cathode compartment. Preferential distribution of Cr accumulations at the cathode air inlet occurs from trapping of Cr species by reactive/protective LSC layers. Samples A1 and A2 were extracted at air inlet and air outlet regions, respectively, for post-analysis purposes.

not found as expected under the combined Cr/S poisoning conditions, but an $Sr(Cr,S)O_4$ compound was identified in both cathode and CCL.

In the present investigation, the focus is placed on the identification of the important factors governing the Cr poisoning of LSM cathodes in the presence of sulfur, by analyzing the chemical form of the Cr phases and their distribution within the cathode layers.

## 2. Materials and methods

This work compares post-test observations from stack testing under combined Cr and S contaminating conditions (hereafter named type A), to those from a button cell (type B) tested under controlled Cr poisoning conditions, without S, in a multicathode configuration.

Both A and B type cells were Ni-YSZ anode-supported with thin 8YSZ electrolyte and $(La,Sr)MnO_3/(Y_2O_3)_{0.08}(ZrO_2)_{0.92}$ (LSM/YSZ) composite cathodes, with slightly different perovskite compositions $(La_{0.75}Sr_{0.25})_{0.95}MnO_{3\pm\delta}$ for type A and $(La_{0.70}Sr_{0.30})_{0.90}MnO_{3\pm\delta}$ for type B, respectively, due to development reasons. The earlier used cathode stoichiometry, used for type A cell, was later found less stable towards zirconate formation than the more recent composition (due to a higher A-site deficiency), which became standard in our activities after cell test A. By the same token, different CCLs were used in both test types: type A cathodes were covered with $(La_{0.8}Sr_{0.2})CoO_3$, type B with LSM (the same stoichiometry as for the active cathode composition). With respect to the contamination issue dealt with in this study, i.e. that in the active cathode region (not CCL), the A and B active cathode compositions can be regarded as close enough for the purpose of comparison, and one can assume that the current collection layer does not significantly alter our conclusions, for the active cathode behavior under combined Cr and S contamination.

Type A cell (200 $cm^2$) was tested for 1900 h at 1073 K on a highly instrumented, so-called segmented, 1-cell stack unit. Owing to the cathode segmentation, Fig. 1, it provided *in situ* local information with time of operation. The test was followed by post-mortem analysis (reported recently in [13,14]) and coupled to model studies of detailed electrochemistry and the generation, transport and deposition of contaminants, which enabled to establish a strong correlation between local performance degradation and distribution of contaminant accumulations [15].

Combined contamination in the type A test was, for Cr, due to stack-upstream alloys (1.4828, 1.4849 and Incoloy800) used to feed hot air, and for S, due to an insulating high-temperature sealing paste (*type1500 Coltogum*, composition: atomic %: 36 Si, 6 Na, 4 Ba, 3 S, 3 Al, 2 Mg, <1 Ca, K, Fe, balance O) used for the galvanic separation between cathode segments, besides $SO_2$ from compressed air.

During operation, Cr vapor species accumulated preferentially at air inlet regions locally causing higher degradation rates. Differences between global and local performance of the cell, polarized with a current density of 0.4 A $cm^{-2}$ around 0.75 V, underlined these findings: air inlet regions showed a higher overpotential (mainly attributed to cathode losses) of ca. 0.35 V compared to the air outlet with only 0.25 V. Contrariwise, as S contamination from the insulating paste is generated within the complete airflow along the cell (due to its segmentation), S accumulations are found equally distributed on the cell; its impact on performance, however, is far less pronounced [15].

Type B cell was smaller (28 $cm^2$) and carried 4 cathode segments of 1 $cm^2$ each (Fig. 1). In this test, NiCrFe alloy (Inconel 602)

**Table 1**
Summary of post-test observations performed on different cathode samples to link sample type and location from Fig. 1 to electron microscopy results from Figs. 2–5. Numbers in brackets refer to previous post-test observations.

| Type | Sample | Location | Observations in this study | Previously reported observations |
|---|---|---|---|---|
| A | A1 | Air inlet | SEM-EDS (Fig. 2)<br>STEM-EDS (Fig. 3)<br>TEM-SAED (Fig. 3)<br>EFTEM | SEM-EDS (cathode) [12]<br>SEM-EDS (CCL) [7,13]<br>TEM-EDS [14,15]<br>XRD (CCL) [13] |
| A | A2 | Air outlet | SEM-EDS (Fig. 2) | SEM-EDS [13]<br>XRD (CCL) [13] |
| Synthesized pellets | $Sr(Cr,S)O_4$ | – | SEM-EDS (Fig. 4)<br>XRD | |
| B | B1 | (Central air feed) | SEM-EDS (Fig. 2)<br>STEM-EDS (Fig. 5) | |

tubing was used for hot air feeding and deliberate generation of volatile Cr species [16]. This cell was operated at 1125 K over 700 h having as scope the evaluation of Mn-doping of the YSZ phase to prevent zirconate formation in the composite cathode but which is not addressed in the present study.

The investigation methods carried out on both A and B cells are summarized in Table 1, including references to the different result figures (Figs. 2–5) in this paper. For the large A type cell, samples from both the air inlet (A1) and air outlet (A2) regions were analyzed (Fig. 1).

In addition to post-test analysis including X-ray diffraction (XRD), energy-dispersive X-ray spectroscopy (EDS) in both scanning and transmission electron microscopes (SEM/TEM) and focused ion beam (FIB) also described in previous publications [13,14,17], selective area electron diffraction (SAED) were performed on a *CM20* TEM (*FEI-Philips*), using *JEMS* software (P. Stadelmann [18]) for diffraction indexing, as well as energy-filtered TEM (EFTEM) with an in-column omega filter on a *Jeol* TEM (*type 2200FS*).

To profile contamination accumulations through the cathode thickness, a methodology based on the quantification of thin cathode slices, extracted from an EDS mapping is used according to our protocol described elsewhere [16] and that can be summarized as follows. To bypass the quantification issue for small Cr quantities within LSM-YSZ composite cathode, due to the strong overlap of the Cr X-ray emission lines with the ones from La, Mn and O, Cr is quantified using an empirical law based on the La $L_{\beta 2.15}/L_{\alpha 1}$ peak height ratio and calibrated on Cr-doped LSM-YSZ standards. Cr within the LSC CCL, as well as S in both cathode and CCL, were quantified using INCA (Oxford Instruments) software.

In addition, also included in Table 1, a Sr/Cr/S-compound was synthesized in a separate experiment in this study, by blending chromium oxide $Cr_2O_3$, strontium carbonate $SrCO_3$ and ammonium sulfate $(NH_4)_2SO_4$ powders (28, 63 and 9 wt%, ratio; all from *Alfa Aesar*) and pressing into pellets. A pellet was sintered at 1473 K for 10 h in stagnant air: these experimental conditions are known to favor the formation of $SrCrO_4$ [19–21]. Resulting reaction phases were crushed in an agate mortar and deposited onto an YSZ plate for analysis purpose.

The main data for thermodynamic analysis of perovskite stability is taken from the thermodynamic database MALT (Materials-oriented Little Thermodynamic database; http://www.kagaku.com/malt). Thermodynamic stability results, under Cr, $SO_2$ and simultaneous Cr and $SO_2$ contaminating conditions, are obtained for $(La_{0.8}Sr_{0.2})_1MnO_3$, $(La_{0.75}Sr_{0.2})_1MnO_3$ and $(La_{0.7}Sr_{0.25})_1MnO_3$ cathode compositions. The latter composition is assumed closest to the actual $(La_{0.75}Sr_{0.25})_{0.95}MnO_{3\pm\delta}$ composition, as this cathode with A-site deficiency has a Sr content around 0.2–0.25. In this analysis, the effect of Cr contamination is evaluated by reaction of 1 mole LSM with 0.1 mole $CrO_3$, although the major gaseous species is $CrO_2(OH)_2$. The effect of S contamination on perovskite compounds is investigated for various $SO_2$ amounts. A prior reading of previous studies from Yokokawa et al. using the MALT database [11] should facilitate the interpretation of the resulting thermodynamic stability graphs.

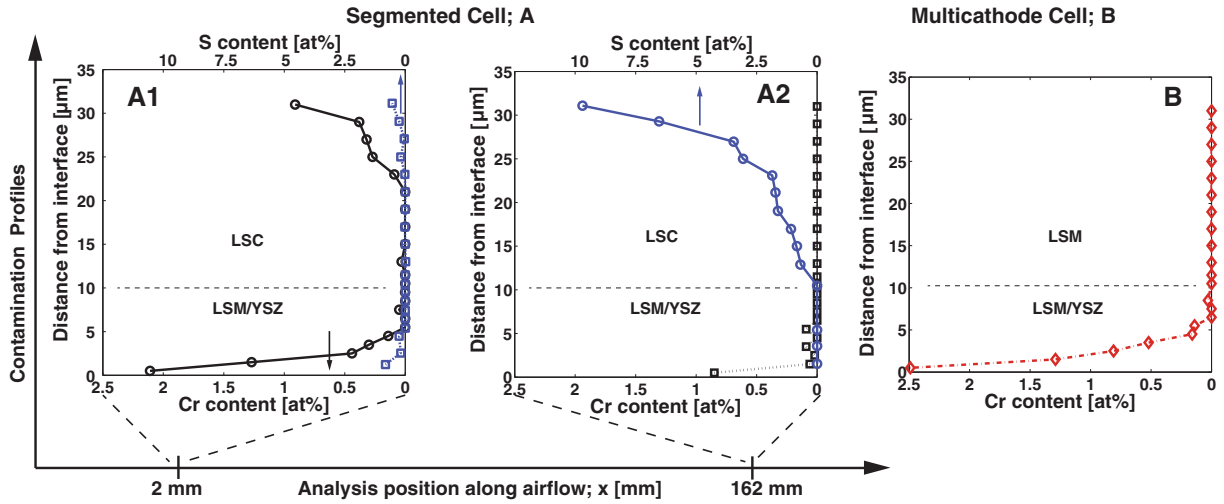


**Fig. 2.** Cr and S contamination profiles for two samples of the segmented cell; samples A1 and A2 stem from air inlet and air outlet regions, respectively. The profiles are obtained by space-averaging EDS data for thin cathode slices. For comparison, a Cr profile of a sample from the multicathode cell, tested under Cr-poisoning conditions only, is shown on the right. For both samples A1 and B, Cr profiles indicate active sites near the electrolyte/cathode interface being polluted by Cr.

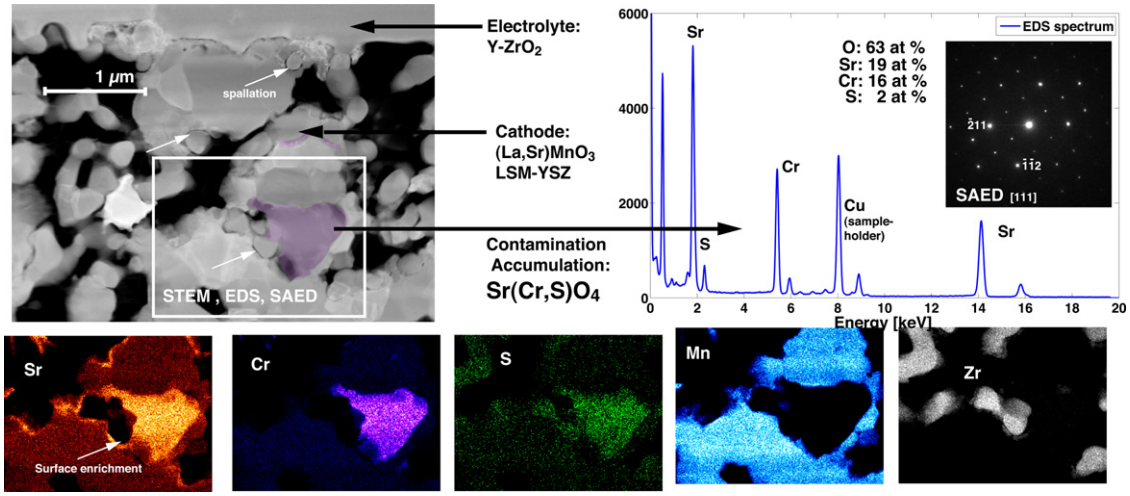


**Fig. 3.** Dark-field scanning-TEM (DF-STEM) imaging of a near-electrolyte cathode region from sample A1. EDS mapping indicates S to be incorporated into the Sr-chromate grain, confirmed by quantification results of the EDS spectrum as well as by the indexation of the diffraction pattern.

## 3. Results: compound identification

This section aims to investigate the effect of the presence of sulfur on the Cr-poisoning mechanism in LSM/YSZ cathodes, by identifying the phase and composition of the Cr deposits. For this purpose, three different cell locations, with differences in the nature and the severity of contamination were investigated, i.e. high Cr and some S for sample A1, high S with minor Cr for sample A2 and Cr without S for sample B1. Fig. 2 compares contamination profiles for samples A1, A2 and B. These cross-section profiles are obtained by an EDS space-averaging technique that is described elsewhere [16] and summarized above.

### 3.1. Chromium contamination

As mentioned in Section 2, Cr contamination is generated by FeCr-alloy compounds located upstream of the cell and exposed to the hot air flux. The gaseous partial pressure of Cr-vapors in the air flow was estimated from oxide scale growth on these high-temperature alloys as well as from the quantification of Cr accumulations in the cell [7]. This value is in agreement with an *in situ* measurement of Cr species [22], which had shown saturation of the air flux with Cr vapors in these testing conditions. A partial pressure of $9 \times 10^{-9}$ atm is therefore expected for $CrO_2(OH)_2(g)$ species at the air entry location of the cell.

Cr accumulations are subsequently found at the electrolyte/cathode interface of sample A1 taken at the air inlet location (cf. Fig. 2; left profile), causing cathode performance degradation

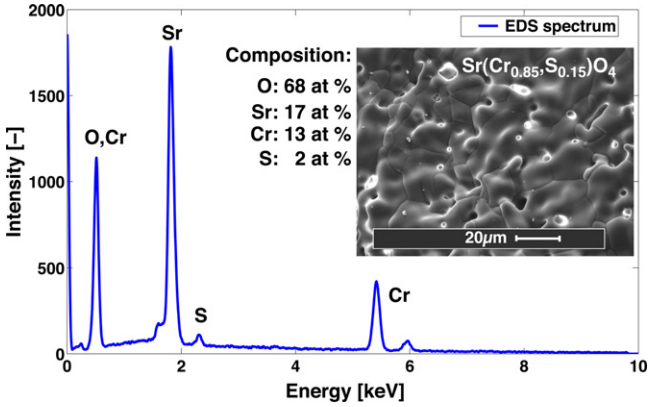


**Fig. 4.** Space-averaged EDS spectrum quantification over some Sr-chromate grains, from a macroscopically yellow region of the sintered Sr/Cr/S-oxide pellet synthesized in this study, suggests the S-added Sr-chromate phase to have a composition close to the compound found in cathode sample A1.

by Cr-poisoning [12]. Further downstream along the air channel, only minor Cr amounts are found, confined to the interface (see Fig. 2; middle profile, sample A2). Part of the Cr contamination is trapped in the LSC CCL, mainly at the surface of this Cr getter layer. The Cr-trapping nature of LSC is underlined by increasing amounts of Cr near the CCL surface (see Fig. 2; left profile) that lies ca. 30 μm distance from the interface. This finding is in agreement with previous observations of the CCL surface, where Cr was found

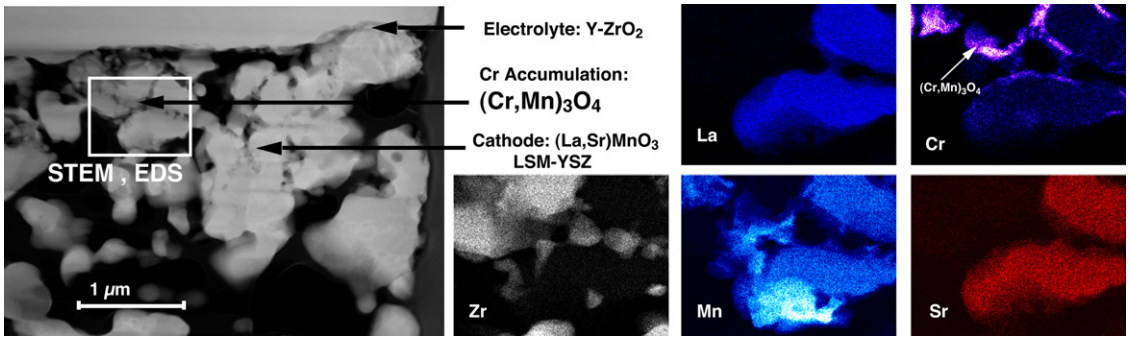


**Fig. 5.** DF-STEM-EDS imaging of a near-electrolyte cathode region from sample B of the multicathode-type cell. Thin Cr accumulations are found along active phase boundaries. Point-analysis of Cr-rich phases indicates a mixed Cr,Mn-oxide composition close to $(Mn,Cr)_3O_4$.

to accumulate in the form of a $SrCrO_4$-related phase [13], as well as with reaction schemes between LSC and acidic pollutant species like Cr described in the literature [23–25]. The Cr-getter effect of LSC thus mitigated the extent of Cr-poisoning in active cathode regions of sample A1. Nevertheless, the amounts of Cr near the interface in sample A1 are found comparable with the value of Cr accumulations for cell B, without LSC CCL but exposed to lower Cr vapor concentrations (Fig. 1); which we believe validates their comparability in this study.

### 3.2. Sulfur contamination

In the case of sulfur contamination (sample A), this experiment did not enable to determine the exact nature and the partial pressure of gaseous S species. The lowest prognosis can be set at the $SO_2$ concentration in environmental air which is around 10 ppb. Additional S contamination, originated from the insulating paste in the vicinity of the cathode segments, is poisoning the cathode (cf. Fig. 2; S profiles) with increasing contamination load along the airflow.

Therefore, highest S-poisoning is found at cathode outlet regions, especially at the LSC CCL surface (cf. Fig. 2; middle profile). Near-electrolyte/cathode interface regions are free of S-poisoning in sample A2, as expected by the nature of the $SrSO_4$ formation reaction (as reported previously [13]), which is oxidative and does not take place at active sites for oxygen reduction [9]. The effect on cathode performance of sulfur alone is thus expected to be small, and further investigations were not undertaken for sample A2.

The amounts of S measured in sample A1 are low, but are close to follow a profile corresponding to Cr accumulations; S deposits are both found on the CCL surface and near the cathode/electrolyte interface. No S is observed, and therefore not reported, for sample B, as was expected and intended. These SEM/EDS observations reported in Sections 3.1 and 3.2 suggest an interaction between the two contaminant species Cr and S. This situation is aimed to be clarified at higher magnification by TEM investigations.

### 3.3. Combined Cr an S contamination: a comparative study between contaminant accumulations in active cathode regions of samples A1 and B

In both samples A1 and B, the active cathode regions are confined to the cathode/electrolyte interface and are poisoned with similar amounts of Cr accumulations. These samples are therefore seen close enough for direct comparison of the Cr deposit's nature to investigate the effect of sulfur presence (sample A1 only) on the Cr-poisoning mechanism.

STEM-EDS observations of a near-interface region of sample A1, shown in Fig. 3, reveal the presence of a Sr/Cr/S-oxide grain within the LSM/YSZ composite cathode. The composition of the grain is identified by EDS as $Sr(Cr_{0.85},S_{0.15})O_4$, in agreement with observations of Sr/Cr/S-phases on the CCL surface published previously [13]. Indeed, always the same composition is measured on multiple analysis locations in both active cathode and CCL surface regions, whereas the impurity levels are very different above/beneath the LSC CCL (see thermodynamic analysis in Section 4.2) given by its trapping property. The following text reports additional proofs of the $Sr(Cr_{0.85},S_{0.15})O_4$ phase within LSM/YSZ near the cathode–electrolyte interface.

EFTEM imaging of the $Sr(Cr,S)O_4$ grain confirms the homogeneous distribution of its constituting elements; the following energies were used for this analysis: Sr (1940 eV), Cr (574 eV), S (228 eV) and O (532 eV). Indexing the electronic diffraction pattern, using JEMS TEM simulation software [18], confirms the compound as monoclinic $SrCrO_4$ with 15% Cr substituted by S.

To further investigate the existence of this phase, a Sr/Cr/S compound was synthesized in the separate experiment by sintering a pellet pressed from the $SrCO_3/Cr_2O_3/(NH_4)_2SO_4$-blend (see Section 2). It macroscopically shows yellow, black and green colors, indicating the presence of $SrCrO_4$, $Sr_3Cr_2O_8$ and unreacted $Cr_2O_3$ [20]. EDS quantification reveals S to be incorporated into both the yellow ($SrCrO_4$), illustrated in Fig. 4, and the black ($Sr_3Cr_2O_8$) structure (not shown here), underlining the S-gettering nature of Sr/Cr-compounds [26].

As previously reported for $SrCrO_4$ compounds found on the CCL surface with identical S incorporation [13] – $SrCrO_4$ is the main reaction product in the LSC-Cr system – [11], shifts in the XRD pattern of $SrCrO_4$ are expected, caused by the radii ratio S/Cr of ca. 0.6. Indeed, the XRD pattern from the synthesized $Sr(Cr,S)O_4$ phase shifts from the ICDD-35743 ($SrCrO_4$) structure towards ICDD-730529 ($SrSO_4$), as reported for the conversion of celestite to Sr-chromate [27].

For sample B, with Cr contamination without the additional presence of S (cf. Fig. 2; right profile), Cr accumulations are found in the form of Cr–Mn-spinel phases as illustrated in Fig. 5. Contrarily to the bulky-chromate grains found for sample A1, the observed Cr accumulations in sample B are distributed as small grains along phase-boundaries.

The observations reported here strongly suggest that the $SrCrO_4$ formation in LSM, although not directly expected from a thermodynamic point of view (cf. Fig. 6a), is enabled by the presence of sulfur dioxide in terms of formation of a solid solution between $SrCrO_4$ and $SrSO_4$ with higher stability in the air inlet location of the type A cell. This formation possibility is strengthened by the more oxidative atmosphere and lower temperature conditions, which are typically observed at the cathode air entry location (cf. Fig. 1; sample A1). $SO_2$ is suggested to act as chromate formation promoter [26] and to incorporate into this phase to form a $Sr(Cr,S)O_4$ compound.

This hypothesis is evaluated here by means of thermodynamic analysis for the different contaminating conditions: Cr only, S only, as well as Cr and S simultaneously. As this post-test analysis comprises a single snapshot after SOFC operation, kinetic considerations of Cr-phase formation cannot be addressed in the present work.

## 4. Discussion: thermodynamic analysis

### 4.1. Cr-LSM reaction

Additional thermodynamic analysis to that published earlier by Yokokawa et al. [11] is shown in Fig. 6, where the temperature dependence of the reaction products between LSM and Cr (0.1 mole $CrO_3$) at $pO_2 = 1$ atm indicates that $SrCrO_4$ formation can take place at the lower temperature region; *n* represents the mole number of each phase formed as a function of temperature and oxygen partial pressure.

At 1073 K, the average operating temperature of the segmented cell A, on the one hand no $SrCrO_4$ is expected; on the other hand 1073 K is close to those temperatures at which $SrCrO_4$ can be formed, and it must be taken into account that the inlet zone (where sample A1 was taken) will be colder than the 1073 K average (by at least 20 °C [15]).

To underline this finding, the thermodynamic activity of plausible reaction products between LSM and Cr, in particular of $SrCrO_4$, is given in Fig. 6c (log-scale) and d (linear-scale). The thermodynamic activity, $a(SrCrO_4)$, is close to unity, i.e. $SrCrO_4$ is formed, in oxidative atmosphere and decreases with decreasing oxygen potential.

Cr,Mn-spinel phases are on the other hand stable at the mean SOFC operating temperature of 1073 K, at low $pO_2$ (Fig. 6b), thus typically under conditions found at active cathode regions, near

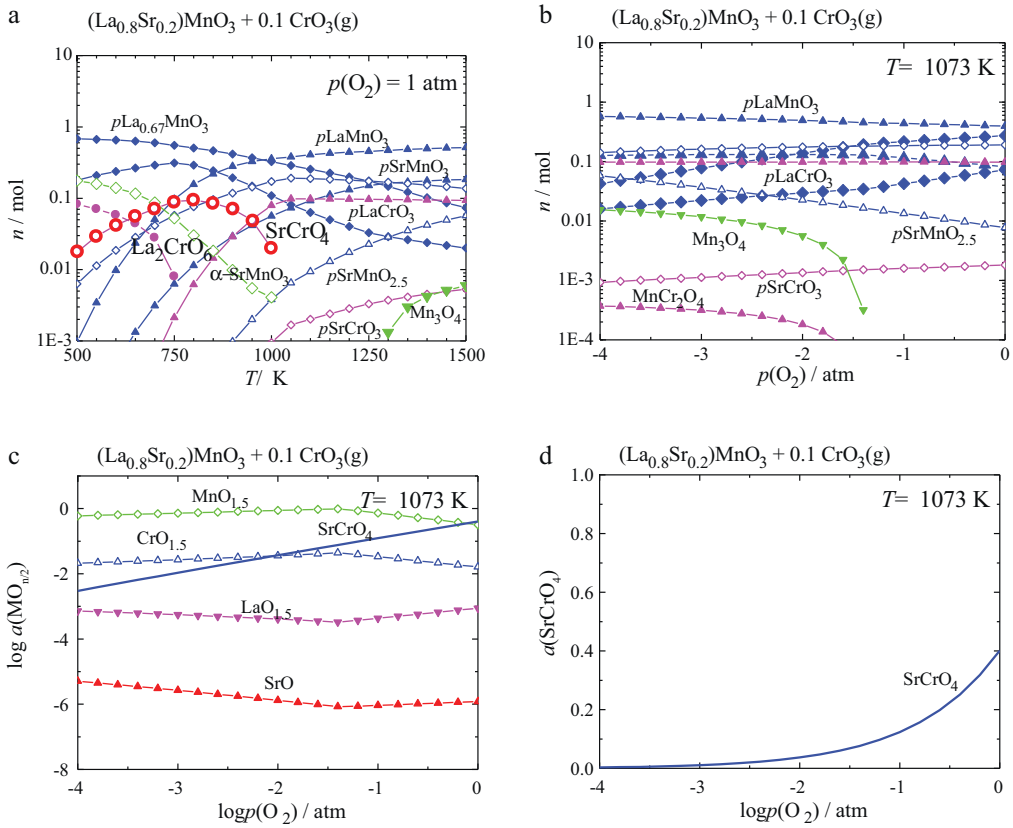


**Fig. 6.** (A) Temperature dependence of the reaction products between 1 mole LSM and 0.1 mole $CrO_3$ at $pO_2 = 1$ atm; $SrCrO_4$ formation takes place at lower temperature regions. (B) $pO_2$ dependence of the reaction products at 1073 K; $MnCr_2O_4$ is formed in the low $pO_2$ region. (C) Oxygen partial pressure dependence of the activity of the reaction products between LSM and Cr. (D) In oxidative atmosphere, the activity of $SrCrO_4$ is close to unity.

the electrolyte/cathode interface where the local overpotential is high, as observed in Fig. 5.

### 4.2. S-LSM and S-LSC reactions

Besides severe sulfur-poisoning in sample A2, S contamination, although in minor extent, is also identified in sample A1 (Fig. 2). Therefore the effect of sulfur on LSM and LSC perovskite cathode layers is investigated to know if and how the LSC CCL traps $SO_2$ before this contaminant reaches the active LSM cathode.

Reactions of LSC from the CCL with $SO_2$ can be separated into three regions (I–III) and described by the following Eqs. (1)–(3), as illustrated in Fig. 7a; the respective equilibrium partial pressures plateaus for $SO_2$ for the three reactions are given in Fig. 7b.

$$\text{Region I}\ (La_{1-y}Sr_y)CoO_3 + ySO_2 = (1-y)LaCoO_3 + ySrSO_4 + yCoO \quad (1)$$

$$\text{Region II}\ (1-y)LaCoO_3 + 0.5(1-y)SO_2 = 0.5(1-y)La_2O_2SO_4 + (1-y)CoO \quad (2)$$

$$\text{Region III}\ CoO + SO_2 + 0.5O_2 = CoSO_4 \quad (3)$$

Similarly, the reactions between LSM and $SO_2$ are described by Eqs. (4)–(7), which are graphically represented in Fig. 7c with the corresponding partial pressure plateaus given in Fig. 7d.

$$\text{Region 0}\ (La_{1-y}Sr_x)MnO_3 = (1-z)(La_{1-y'}Sr_{x'})MnO_3 + z\alpha\text{-}SrMnO_3 \quad (4')$$

$$z\alpha\text{-}SrMnO_3 + z(SO_2 + O_2) + (1-z)(La_{1-y'}Sr_{x'})MnO_3 = zSrSO_4 + (La_{1-y}Sr_{x-z})MnO_3 \quad (4)$$

$$\text{Region I}\ (La_{1-y}Sr_{x-z})MnO_3 + (x-z)SO_2 + dO_2 = (1-x+z)La_{(1-y)/(1-x+z)}MnO_3 + (x-z)SrSO_4 + (1/3)(x-z)Mn_3O_4 \quad (5)$$

$$\text{Region II}\ (1-x+z)La_{(1-y)/(1-x+z)}MnO_3 + 0.5(1-y)SO_2 + dO_2 = 0.5(1-y)La_2O_2SO_4 + (1/3)(1-x+z)Mn_3O_4 \quad (6)$$

$$\text{Region III}\ (1/3)Mn_3O_4 + SO_2 + (1/3)O_2 = MnSO_4 \quad (7)$$

This reaction scheme indicates the alpha-$SrMnO_3$ phase to be precipitated from LSM even without $SO_2$ gas in the air; this is due to the A-site deficiency of the LSM perovskite composition (cf. Eq. (4′)). However, in practice, the precipitation of alpha-$SrMnO_3$ is not observed and the reaction of LSM with $SO_2$ first yields $SrSO_4$ alone without precipitation of manganese oxides. This precipitation is expected to be kinetically hindered, comparable to pyrochlore phase formation between LSM and YSZ that also results without the precipitation of manganese oxides. No Region O is observed for LSC in Fig. 7a, due to its stoichiometry (no A-site deficiency).

Regions I–III present similar reaction paths leading to $SrCrO_4$ formation (Region I) and other phases (Regions II and III) in LSM-$SO_2$ and LSC-$SO_2$ systems. Differences in $SO_2$ equilibrium pressures are found for these regions and the two perovskites; they are generally lower (i.e. more reactive) for LSC reactions compared to those

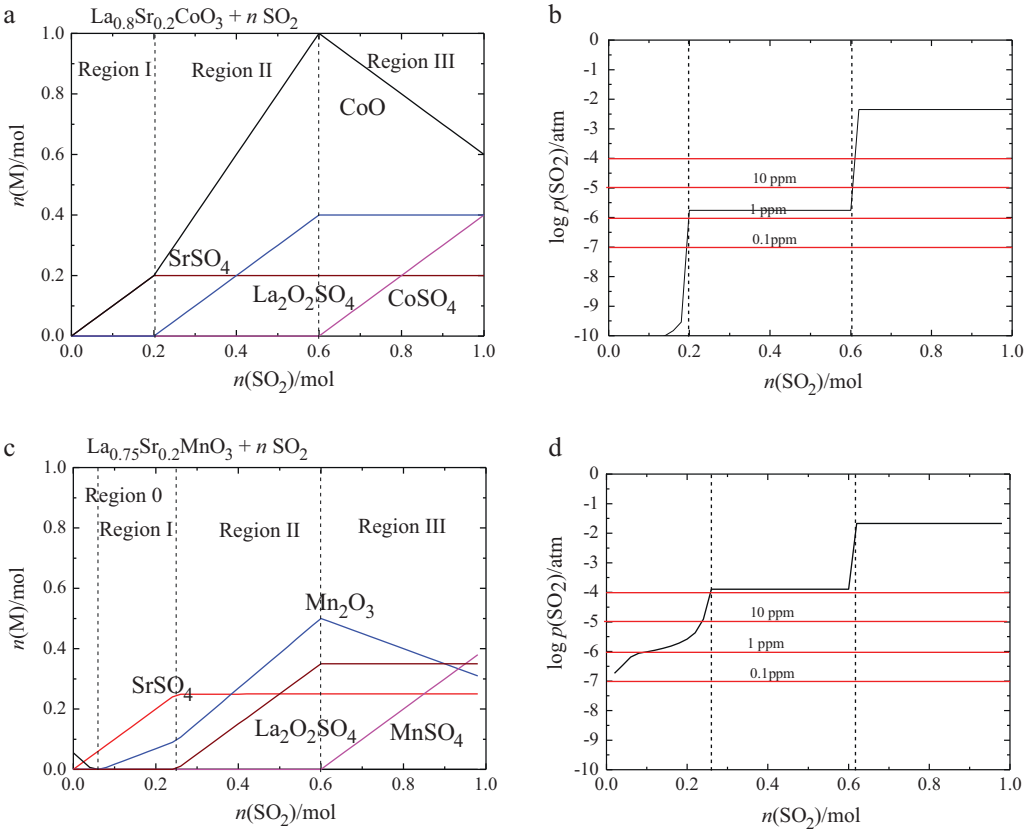


**Fig. 7.** (A) LSC reaction with $SO_2$; Regions I, II and III correspond to Eqs. (1), (2) and (3), respectively. (B) The equilibrium partial pressures of $SO_2$ for respective reaction Eqs. (1)–(3). (C) LSM reaction with $SO_2$; Regions O–III correspond to Eqs. (4)–(7). (D) Equilibrium partial pressure for $SO_2$ in Regions I–III.

for LSM, i.e. four orders of magnitude between LSM and LSC systems for the $SrSO_4$ formation (Region I), below two orders of magnitude in the Region II for the $La_2O_2SO_4$ formation, and below one order in Region III, for Mn- or Co-sulfate formation.

The partial pressure of $SO_2$ in the type A cell test being unknown, a lower and a higher level case is considered. Considering also these two materials not individually but in cell configuration with LSC on top of the LSM cathode, where the LSC CCL is thought to act as an $SO_2$ getter, the above findings, in particular for Fig. 7, indicate the following:

i) With a partial pressure of $SO_2$ lower than 1 ppm, nearly all $SO_2$ is captured by LSC in the CCL to form $SrSO_4$ (LSC-Region I, Fig. 7b). The remaining $SO_2$ passing through this trapping layer has a partial pressure of around $10^{-10}$ atm. The amount of sulfur reaching the cathode is therefore too low to affect LSM. The LSC protects the active cathode region unless the trapping layer becomes saturated.
ii) When the $SO_2$ partial pressure is between 1 and 500 ppm, LSC is decomposed into $SrSO_4$ and $LaCoO_3$ (LSC-Region II, Fig. 7b); the trapping effect of $LaCoO_3$ reduces the $SO_2$ partial pressure to a level of 1 ppm. This remaining amount of $SO_2$ penetrates until the active cathode regions and reacts with LSM according to reaction Eqs. (4) and (5) (LSM-Regions O and partly I, Fig. 7d). In such cases, up to 0.1 mole of $SO_2$ can react with one mole of LSM to form $SrSO_4$.

### 4.3. Cr/S-LSM reactions

As it was shown that up to 1 ppm $SO_2$ can react with active cathode regions exposed to high $SO_2$ contamination, the effect of Cr on LSM in simultaneous S contaminating conditions is therefore considered as follows (Fig. 8):

1st case: 1 mole LSM + 0.1 mole $CrO_3$: the reaction between LSM and $CrO_3$(g) favors Cr absorption into the B-site of the perovskite lattice. The A-site deficiency of LSM limits on the one hand the amount of Cr to be integrated into the perovskite lattice, but favors on the other hand the precipitation of manganese oxides. $SrCrO_4$ is not formed in LSM as this composition is the most stable among La,Sr-based perovskite compounds.

Chemical reactivity and electrochemical degradation are however not necessarily in relation as the chemically stable LSM suffers most from Cr-poisoning by other means than the $SrCrO_4$ formation, namely the preferential deposition of Cr species at active sites for oxygen reduction.

Two Cr-deposition descriptions for Cr-poisoning in LSM-YSZ composite cathodes are found in literature [26,28]; by the direct electrochemical reduction of $Cr^{(VI)}$ to $Cr^{(III)}$ (cf. Eq. (8)), or via $Mn^{(II)}$, generated in LSM under polarization, as nucleation sites (cf. unbalanced Eqs. (9) and (10)).

$$CrO_2(OH)_{2(g)} + 3/2\,V_O^{\bullet\bullet} + 3e^- \leftrightarrow 1/2Cr_2O_{3(s)} + H_2O_{(g)} + 3/2O_O^x \quad (8)$$

$$CrO_2(OH)_{2(g)} + Mn^{2+}{}_{(s)} + e^- \leftrightarrow Cr\text{–}Mn\text{–}O_{nucleus} + H_2O_{(g)} \quad (9)$$

$$Cr\text{–}Mn\text{–}O_{nucleus} + CrO_2(OH)_{2(g)} \leftrightarrow Cr_2O_{3(s)} + H_2O_{(g)} + Mn^{4+}{}_{(s)} + e^- \quad (10)$$

Either way, $Cr_2O_3$ reacts with LSM to form the $(Cr,Mn)_3O_4$ spinel phase, which is the thermodynamically favored phase, at active sites for oxygen reduction where $pO_2$ is low (cf. Figs. 6b and 8a),

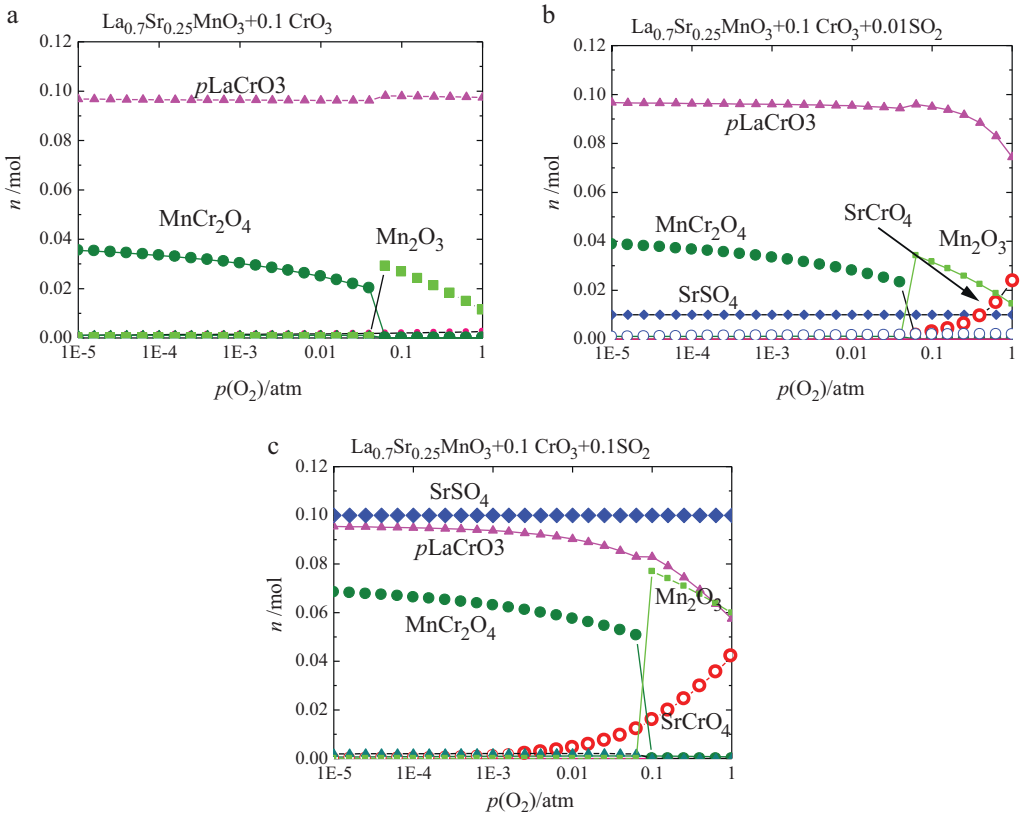


**Fig. 8.** (A) Reaction products between 1 mole LSM and 0.1 mole $CrO_3$ according to different oxygen partial pressures; Cr integration into the B-site of LSM perovskite lattice is thermodynamically favored. (B) Reaction products between LSM, Cr and 0.01 mole $SO_2$; minor amounts of $SrCrO_4$ and $SrSO_4$, compared to Cr B-site integration, are formed. (C) Reaction of LSM with Cr and high S contents yields to the formation of $SrCrO_4$, $SrSO_4$ and increased amounts of precipitated Mn-oxides.

and which is found to be formed at the active phase boundaries, as illustrated in Fig. 5.

2nd case: 1 mole LSM + 0.1 mole $CrO_3$ + 0.01/0.1 mole $SO_2$ (Fig. 8b and c): when sulfur contamination occurs at the same time as Cr-poisoning, $SrSO_4$ is formed depending on the sulfur contamination level. This $SrSO_4$ formation enhances the formation of a solid solution between $SrCrO_4$ and $SrSO_4$; an ideal solid solution is assumed in the thermodynamic analysis. The amount of precipitated Mn oxides also increases, due to the decrease in the A-site occupancy in the perovskite lattice (Sr-consumption by chromate and sulfate formation), leading to a decreased mole number of the perovskite lattice.

### 4.4. Contamination effect on cell performance

Thermodynamic analysis, predicting the co-existence of $SrSO_4$ and $SrCrO_4$ phases in LSM (cf. Fig. 8b and c), with the assumption that these two phases form a solid-solution, is consistent with the observed formation of S-added Sr-chromate. The effect of combined Cr and S contaminating conditions in terms of cathode performance degradation is now evaluated as follows:

$SrCrO_4$ is (and $Sr(Cr,S)O_4$ is expected to be) poorly conductive and reduces the cathode porosity [11]. Impurities like S can enhance sintering leading to morphological changes [26]. Similarly, cation-depletion of LSM, after Sr consumption, favors perovskite coarsening. $SrCrO_4$ has a high thermal expansion coefficient (ca. $17.5 \times 10^{-6}\,K^{-1}$), and could therefore induce spallation between the different phases during thermal changes, especially in coarsened microstructures [19] as observed in Fig. 3. In addition, the depletion of Sr in LSM leads to a change of the perovskite thermal expansion coefficient. In summary, $Sr(Cr,S)O_4$ formation can possibly induce a delayed deleterious effect on the cathode performance, whereas the immediate effect, i.e. sparse and bulky chromate formation (cf. Fig. 3), is expected to be smaller compared to the formation of Cr/Mn-oxides along the triple-phase-boundaries (cf. Fig. 5) in Cr-poisoning conditions [11].

Here, the total accumulated Cr amount for type A cell ($18\,\mu g\,cm^{-2}$ for cathode and CLL per 1 kh operation) and the observed performance degradation (ca. $1\%\,kh^{-1}$) [7] indicates serious cathode poisoning, comparable with findings from cell endurance testing performed elsewhere [29] ($15\,\mu g\,cm^{-2}$ for tests with less than $1.5\%\,k\,h^{-1}$ degradation [7]). The important difference between global and local degradation rates of a repeat-element suggests however that correlations can only be done between local distribution of pollutant species and the causes of local degradation rates [12], i.e. locally high performance degradation rates at the air inlet regions are consistent with the localization of high contamination accumulation, whereas the main part of the type A cell remained free of degradation-causing contamination.

The actual amount of the $Sr(Cr,S)O_4$ phase in the cathode, by its conductivity decrease and grain spallation contribution, cannot directly be linked to the observed decrease of local power density. The complexity of superimposed degradation effects, not limited to Cr and S (e.g. a silicon-poisoning was observed on the same cell [17]), precludes such direct correlations. A different situation is expected from type B cell, with only Cr accumulation near the cathode–electrolyte interface. From a multicathode-cell test [16] performed in identical conditions than for cell type B, we can derive that the Cr amounts observed in sample B1 should be correlated to a degradation rate of $2.5–3\%\,k\,h^{-1}$. The observed degradation was, with ca. 5% voltage decay after 700 h of testing, actually higher; the

added Mn-oxide, introduced by Mn-doping of the YSZ-electrolyte, in the test of Ref. [16], likely changed Cr-deposition mechanisms (cf. Eqs. (9) and (10)) and caused additional superimposed degradation [30].

## 5. Conclusions

The present study reveals SOFC cathode poisoning mechanisms in the case of chromium contaminating conditions in combination with high sulfur concentrations.

This special case of pollution, far above trace $SO_2$ levels in air, is not a generic situation in SOFC operation but can be representative of accelerated testing. Indeed, S-rich Sr-chromate compounds are frequently observed in LSCF-cathodes after long-term (10,000 h) SOFC operation, where S contamination arises from environmental air. Our observations especially point out the possibility of multiple or combined poisoning phenomena, which lead to interdependent or superimposed degradation effects, hence complicating quantitative correlations between contamination amounts and degradation rates.

In many studies facing the Cr-poisoning phenomenon, different contamination levels, not limited to Cr alone, are suggested to be at least partially responsible for disagreements in the literature related to Cr accumulations. Such differences in contamination can also mitigate the severity of Cr-poisoning.

Finally, this study suggests to carefully select SOFC proximal components to limit S contamination to only the trace amounts vehicled by environmental air.

## Acknowledgements

The Swiss Federal Energy Office (Contract 153569 – AccelenT), as well as the European Commission (FP6 contract SES6-019875 – Flame-SOFC) are gratefully acknowledged for financial support. Antonin Faes and Fabienne Bobard are warmly thanked for TEM-lamellae preparation; Nicola Accardo is acknowledged for the chromate synthesis.

## References

[1] D.B. Meadowcroft, Nature 226 (1970) 847.
[2] W.F. Libby, Science 171 (1971) 499.
[3] I. Rosso, E. Garrone, F. Geobaldo, B. Onida, G. Saracco, V. Specchia, Appl. Catal., B 30 (2001) 61.
[4] H. Wang, Y. Zhu, R. Tan, W. Yao, Catal. Lett. 82 (2002) 199.
[5] L. Wan, in: L.G. Tejuca, J.L.G. Fierro (Eds.), Properties and Applications of Perovskite-Type Oxides, Marcel Dekker Inc., New York, 1993, 145 pp.
[6] Y. Matsuzaki, I. Yasuda, Solid State Ionics 132 (2000) 261.
[7] J.A. Schuler, C. Gehrig, Z. Wuillemin, A.J. Schuler, J. Wochele, C. Ludwig, A. Hessler-Wyser, J. Van herle, J. Power Sources 196 (2011) 7225.
[8] K. Yamaji, Y. Xiong, M. Yoshinaga, H. Kishimoto, M.E. Brito, T. Horita, H. Yokokawa, J. Akikusa, M. Kawano, ECS Trans. 25 (2009) 2853.
[9] Y. Xiong, K. Yamaji, T. Horita, H. Yokokawa, J. Akikusa, H. Eto, T. Inagaki, J. Electrochem. Soc. 156 (2009) B588.
[10] R.R. Liu, S. Taniguchi, Y. Shiratori, K. Ito, K. Sasaki, ECS Trans. 35 (2011) 2255.
[11] H. Yokokawa, T. Horita, N. Sakai, K. Yamaji, M.E. Brito, Y. Xiong, H. Kishimoto, Solid State Ionics 177 (2006) 3193.
[12] Z. Wuillemin, A. Nakajo, A. Müller, J.A. Schuler, S. Diethelm, J. Van herle, D. Favrat, ECS Trans. 25 (2009) 457.
[13] J.A. Schuler, Z. Wuillemin, A. Hessler-Wyser, J. Van herle, ECS Trans. 25 (2009) 2845.
[14] A. Hessler-Wyser, Z. Wuillemin, J.A. Schuler, A. Faes, J. Van herle, J. Mater. Sci. 46 (2011) 4532.
[15] Z. Wuillemin, EPFL PhD Thesis No. 4525, Lausanne, Switzerland, 2009.
[16] J.A. Schuler, P. Tanasini, A. Hessler-Wyser, C. Comninellis, J. Van herle, Electrochem. Commun. 12 (2010) 1682.
[17] J.A. Schuler, Z. Wuillemin, A. Hessler-Wyser, J. Van herle, Electrochem. Solid State Lett. 14 (2011) B20.
[18] P.A. Stadelmann, Ultramicroscopy 21 (1987) 131.
[19] M. Mori, Y. Hiei, N.M. Sammes, Solid State Ionics 135 (2000) 743.
[20] K.T. Jacob, K.P. Abraham, J. Phase Equilib. 21 (1999) 46.
[21] T. Baikie, Z. Ahmad, M. Srinivasan, A. Maignan, S.S. Pramana, T.J. White, J. Solid State Chem. 180 (2007) 1538.
[22] J.A. Schuler, A.J. Schuler, Z. Wuillemin, A. Hessler-Wyser, C. Ludwig, J. Van herle, ECS Trans. 35 (2011) 2001.
[23] D.O.E. Armstrong, D. Jung, C. Kan, E. Wachsman, ECS Trans. 25 (2009) 2871.
[24] H. Yokokawa, N. Sakai, T. Horita, K. Yamaji, M.E. Brito, H. Kishimoto, J. Alloys Compd. 152 (2008) 41.
[25] C. Tofan, D. Klvana, J. Kirchnerova, Appl. Catal., B 36 (2002) 311.
[26] H. Yokokawa, H. Kishimoto, K. Yamaji, T. Horita, ECS Trans. 25 (2009) 401.
[27] J.C. Rendon-Angeles, Y.M. Rangel-Hernandez, J. Lopez-Cuevas, M.I. Pench-Canul, Z. Matamoros-Veloza, K. Yanagisawa, Proc. Int. Conf. on High Press. Sci. Tech. T13, 2005, p. O144.
[28] S.P. Jiang, S. Zhang, Y.D. Zhen, J. Electrochem. Soc. 153 (2006) A127.
[29] N.H. Menzler, I. Vinke, H. Lippert, ECS Trans. 25 (2009) 2899.
[30] P. Tanasini, EPFL PhD Thesis No. 5004, Lausanne, Switzerland, 2011.